

Large-eddy simulation of shallow turbulent wakes behind a conical island F

Cite as: Phys. Fluids **29**, 126601 (2017); <https://doi.org/10.1063/1.5004028>

Submitted: 10 September 2017 . Accepted: 14 November 2017 . Published Online: 11 December 2017

 Pablo Ouro, Catherine A. M. E. Wilson, Paul Evans, and Athanasios Angeloudis

COLLECTIONS

F This paper was selected as Featured



View Online



Export Citation



CrossMark

ARTICLES YOU MAY BE INTERESTED IN

[Development of vortex structures in the wake of a sharp-edged bluff body](#)

Physics of Fluids **29**, 125103 (2017); <https://doi.org/10.1063/1.5003114>

[Dependence of square cylinder wake on Reynolds number](#)

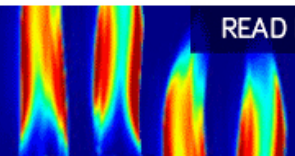
Physics of Fluids **30**, 015102 (2018); <https://doi.org/10.1063/1.4996945>

[Hairpin vortex organization in wall turbulence](#)

Physics of Fluids **19**, 041301 (2007); <https://doi.org/10.1063/1.2717527>

AIP Advances
Fluids and Plasmas Collection

READ NOW



Large-eddy simulation of shallow turbulent wakes behind a conical island

Pablo Ouro,^{1,a)} Catherine A. M. E. Wilson,^{1,b)} Paul Evans,^{2,c)} and Athanasios Angeloudis^{3,d)}

¹Hydro-Environmental Research Centre, School of Engineering, Cardiff University, Cardiff, United Kingdom

²Intertek Energy and Water Consultancy Services, Cardiff, United Kingdom

³Applied Modelling & Computation Group, Department of Earth Science and Engineering, Imperial College London, London, United Kingdom

(Received 10 September 2017; accepted 14 November 2017; published online 11 December 2017)

Large-Eddy Simulations (LESs) and experiments were employed to study the influence of water depth on the hydrodynamics in the wake of a conical island for emergent, shallow, and deeply submerged conditions. The Reynolds numbers based on the island's base diameter for these conditions range from 6500 to 8125. LES results from the two shallower conditions were validated against experimental measurements from an open channel flume and captured the characteristic flow structures around the cone, including the attached recirculation region, vortex shedding, and separated shear layers. The wake was impacted by the transition from emergent to shallow submerged flow conditions with more subtle changes in time-averaged velocity and instantaneous flow structures when the submergence increases further. Despite differences in the breakdown of the separated shear layers, vortex shedding, and the upward flow region on the leeward face (once the cone's apex is submerged), similar flow structures to cylinder flow were observed. These include an arch vortex tilted in the downstream direction and von Karman vortices in the far-wake. Spectra of velocity time series and the drag coefficient indicated that the vortex shedding was constrained by the overtopping flow layer, and thus the shedding frequency decreased as the cone's apex became submerged. Finally, the generalised flow structures in the wake of a submerged conical body are outlined. © 2017 Author(s). All article content, except where otherwise noted, is licensed under a Creative Commons Attribution (CC BY) license (<http://creativecommons.org/licenses/by/4.0/>). <https://doi.org/10.1063/1.5004028>

I. INTRODUCTION

In open channel flows, most turbulent shallow wakes are generated by three-dimensional (3D) obstacles, such as boulders, bridge piers, islands, screens, and plants. However, two-dimensional (2D) bodies such as plates, cylinders, and cuboids have been studied to a greater extent, presumably due to their simplicity and industrial relevance.¹ Therefore, understanding the flow features and wake structures behind these 3D obstructions enables a better understanding of fish and benthic habitats, as well as the transport of sediments, nutrients, and pollutants in rivers, estuaries, and coastal waters.

Shallow flow around emergent (projecting through the water surface) 2D obstacles of varying aspect ratio (h/D ratio, where h is the height and D is the width) and stages of wake development has received much attention (e.g., Refs. 2–4). However, fewer studies have examined the impact of the flow structure in the near-wake region when the obstruction is completely submerged with the flow overtopping the tip of the obstruction,^{1,5,6} a condition relevant to river engineering, coastal engineering, and wind engineering. For such emergent flows, the wake characteristics and flow patterns are dependent on the aspect ratio and Reynolds number. For the case of circular cylinders under high Reynolds number ($Re_D > 10^4$)

flow conditions, these have been classified into three types: (i) a von Karman vortex street shedding mechanism with unsteady separation at the cylinder; (ii) an unsteady wake bubble with a recirculating bubble attached to the cylinder that becomes unstable and oscillates further downstream; and (iii) a steady bubble without instabilities or oscillation.² These classifications are specific to shallow wakes where the transverse object dimension is greater than the flow depth, and the developed large-scale structures are predominantly 2D. The location and strength of turbulent structures are dependent on the Reynolds number, e.g., the horseshoe vortex formed at the upstream cylinder base/bed junction increases in strength, shifts in position, and reduces in area with increasing Reynolds number.⁷

In submerged conditions, the presence of the free-end and the overtopping surface flow layer introduces three-dimensionality to the flow field due to its interaction with the object's sides. Streamwise tip vortices formed off the free-end of the obstacle have been observed for a variety of object shapes and profiles.^{5,8–11} These vortices shift downwards with the downwash flow,⁵ and for the case of cylinders with smaller aspect ratios, they occupy a greater proportion of the water column and therefore dominate the turbulence structures, which prevents the development of von Karman vortex shedding.¹ Hence, in the case of flow around cylinders, vortex shedding appears to be a function of the object's aspect ratio.^{5,8}

The critical aspect ratio at which vortex shedding is suppressed for a cylinder is around three.^{8,12} The drag coefficient and Strouhal number are significantly reduced at an aspect ratio

^{a)}ourobap@cardiff.ac.uk

^{b)}wilsonca@cardiff.ac.uk

^{c)}paul.evans@intertek.com

^{d)}a.angeloudis06@imperial.ac.uk

of around two or three due to free end effects.¹² With increasing aspect ratios, the Strouhal number has been observed to remain constant.¹² For larger ratios ($h/D \geq 9$), periodic shedding and vortex sheets have been observed in the wake over the majority of the cylinder height, with the vertical axis of the vortex sheet no longer parallel to the cylinder axis.¹² This is thought to be due to the interaction of the tip vortices with the vortex shedding at the cylinder mid-height.^{12–14} The vortex sheet axis becomes less inclined further away from the cylinder's free end.¹² The cylinder aspect ratio has also been observed to govern the occurrence of “symmetrical” vortex shedding ($h/D > 2$) rather than the alternate shedding of a vortex from each cylinder side⁵ when the height is significantly greater than the diameter ($h \gg D$).

For a submerged cuboid, the aspect ratio governs the degree of interaction between the horseshoe vortex and the wake region. For smaller aspect ratio objects, such as a cube where $h/D < 6$, the flow is dominated by the interaction of the horseshoe vortex, corner vortices, and the impinging shear layer in the wake. However, for larger aspect ratios (e.g., a rib), the effect of the horseshoe vortex is only observed at the edges of the wake region and has a minimal effect on the centre of the wake.¹⁵ The proportion of flow overtopping and traveling around the object influences the length of the recirculation zone. In the case of a rib, a greater volume of flow travels over the object than around it, and hence the recirculation zone is lengthened when compared to a cube, which has a relatively greater amount of flow deflected around its sides, shortening the recirculation zone.¹⁵ This results in the free-shear layer reattaching at a quicker rate downstream. In submerged cylinder flows, a series of arch vortices are formed immediately downstream of the object within the recirculation region, bounded by the object sides, and the horseshoe vortex. Such arch vortices have been observed for a number of object geometries, including cylinders, hemispheres, ellipsoids, and cubes.^{1,15–17} For the case of cylinders, it has been postulated that the arch vortex is the result of the two tip vortices combining with the vortex sheets shedding from the sides of the obstacle.^{13,18,19} The arch vortex is formed independently of whether the vertical vortices are shed simultaneously from each side of the cylinder or shed off each alternate side as in “von Karman-type” shedding.¹³

A few studies have examined how subtle changes in the cross-sectional profile can affect the wake structure. In deeply submerged flows, Large-Eddy Simulations (LESs) demonstrated that the tip vortices and recirculation bubbles at a cylinder's free-end are not significantly affected by the presence of a vertical plate attached to the downstream side of the cylinder and only the arch vortex and horseshoe vortex were affected.¹⁰ For a cuboid whose upstream and leeward profiles were modified by adding a wedge and elliptical profiles, respectively, LES and experimental data have shown that the upstream face significantly impacts the attachment of overlying flow over the free-end and the flow structure of the magnitude of the downwash flow.²⁰ Furthermore, it was found that the interaction between the tip and lateral vortices was the greatest for the square cylinder without an upstream wedge profile or a leeside elliptical profile, resulting in a strong detachment of flow over the top of the body. The presence of the

elliptical afterbody and the interaction between the tip vortices and side vortices weakened the downwash flow. An ellipsoid with a longer length in the streamwise direction compared to the transverse direction results in more dominant tip structures, while base structures were more dominant in the transverse ellipsoid.¹⁷

Other studies have examined the ratio of flow depth (H) to object height H/h (also termed submergence or relative submergence) with the majority of research focusing on deeper flows usually conducted in wind tunnels. For hemispherical and cylindrical objects, two distinct wake types are observed, both dependent on submergence: a wake-bubble with downstream vortex shedding for slightly submerged and emergent objects²¹ and an enclosed recirculation region with no shedding for moderate to deeply submerged objects.^{16,21} Increasing submergence reduced the vertical extent of the wake region for both conical and hemispherical objects.^{16,22} Furthermore, increasing submergence led to a shorter recirculation length due to the stronger downwash flow re-attaching with the wake flow at a quicker rate.^{16,21,23} For a submerged ellipsoid, the strength of the base vortices reduces with increasing submergence, while the strength of the tip vortices is not affected by submergence.¹⁷ However, the strength of the von Karman-type vortex shedding was highly influenced by the degree of submergence with a wider wake region and stronger periodic shedding taking place for lower submergences.²⁴ In contrast, increasing submergence the region narrows with the eventual termination of the shedding.²⁴

The flow around submerged bluff bodies is largely dominated by energetic flow structures and significant flow separation which constitutes a challenge for numerical modeling. LES has been widely used to study submerged cylinders^{1,25} due to its ability to resolve complex phenomena such as energetic large-scale structures, flow separation at the top of the upstream face,^{6,19} or tip vortices.¹⁰ With the exception of the aforementioned studies, there is a scarcity of experimental and numerical studies examining the wakes of submerged obstacles in shallow flows despite their importance in hydraulic and geophysical contexts.²⁶ Furthermore, the majority of studies have focused on cylinders, cubes, or hemispheres with few studies examining other cross-sectional shape geometries pertinent to river or oceanic flows.

In this study, the near-wake structure in the lee of a conical island is investigated using LES and open channel flume experiments. An LES approach is employed to investigate the time-averaged velocity field and instantaneous turbulent structures for three levels of submergence: (i) emergent (surface-piercing), (ii) shallow submergence, and (iii) deep submergence. The model is first validated against experimental data for both emergent and shallow submerged conditions and then applied to a deeper submergence case to better understand how conical island submergence impacts time-averaged flow properties and instantaneous flow structures in its wake.

II. EXPERIMENTAL SETUP

The experiments were conducted in a recirculating flume of rectangular cross section with glass sidewalls and bed in the hydraulics laboratory at Cardiff University. The flume was

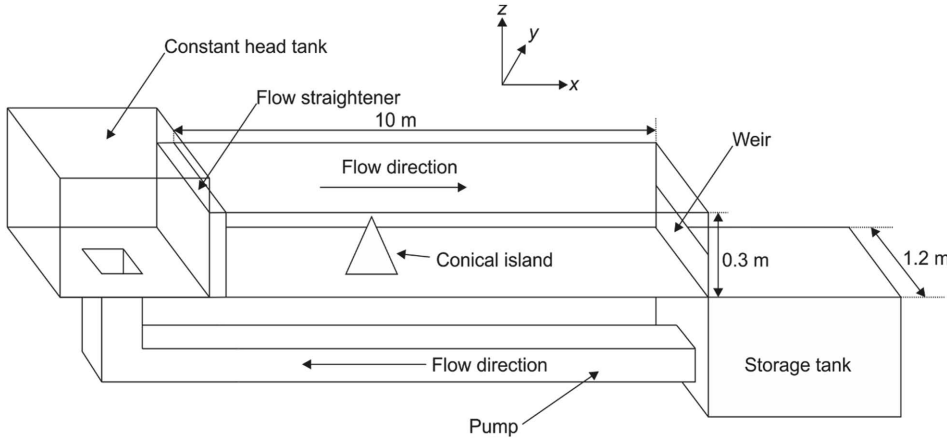


FIG. 1. Schematic diagram of the flume setup including a coordinate system, where x is the longitudinal direction, y is the lateral direction, and z is the vertical direction.

TABLE I. Flow characteristics of the analyzed cases.

Case	H (m)	H/h	Q ($\text{m}^3 \text{s}^{-1}$)	U_0 (m s^{-1})	D/H	$Re_{D_{0.5}}$	Fr
Surface-piercing (SP)	0.110	0.96	0.0133	0.1000	0.68	8125	0.0962
Slightly submerged (SS)	0.142	1.24	0.0133	0.0800	0.88	6500	0.0678
Deeply submerged (DS)	0.220	1.92	0.0266	0.1007	1.35	8206	0.0686

10 m long, 1.2 m wide, and 0.3 m deep (see Fig. 1). The centre-point of the conical island's base was located 3.5 m downstream of the inlet along the centreline of the flume. The conical island was scaled from a natural pinnacle known as Horse Rock, which is located within a tidal strait between Ramsey Island and the mainland of Pembrokeshire in southwest Wales, UK (see Ref. 27 for more details). The island was constructed from stainless steel with a base diameter (D) of 0.1625 m, a height (h) of 0.115 m, and a side slope of 55° to the horizontal. The diameter at the cone's mid-height ($D_{0.5} = D/2$) was 0.081 m. In the experimental investigation, two submergence conditions were examined: $H/h = 0.96$ and $H/h = 1.24$, where H denotes the water depth (see Table I). These conditions represent the minimum and maximum relative submergence levels of Horse Rock during a typical spring tide. The Reynolds numbers based on the cone's diameter at mid-height ($D_{0.5}$) were 6500 and 8125 for the submerged and surface-piercing conditions, respectively. For cylinder wake flows, this corresponds to the region where with increasing Reynolds number, the contribution of the wake turbulence level to the total turbulence level decreases and thus the cylinder drag decreases.²⁸

Time series velocity measurements were collected using a profiling 10-MHz Vectrino II acoustic Doppler velocimeter (ADV) manufactured by Nortek, with a sampling rate of 100 Hz and a sampling time of 150 s. The Vectrino II was configured to sample over a 35 mm range (40-75 mm) using a 1 mm cell size and a 6 mm diameter sampling volume. The signal-to-noise ratio (SNR) and correlation (COR) values were set to the thresholds of >20 dB and $>70\%$, respectively, which was achieved by seeding the water with 10 μm mean diameter silicate powder (density of 1.1 kg m^{-3}). The Phase-Space Thresholding (PST) method of Goring and Nikora²⁹ was employed for despiking the velocity time series. Furthermore, identification of pulse-to-pulse interference (also known

as weak spots), which is an issue related to the spatial separation between the pulse pairs transmitted by the Vectrino profiler, was achieved by examining the velocity variance. These data points were removed from the dataset. An ADV measurement grid resolution of 25 mm was used in both the longitudinal (x) and lateral (y) directions in the vicinity of the obstruction in order to capture the detailed wake velocity structure. As the distance from the conical island increased in the downstream direction, the spacing of the measurements, both longitudinally and laterally, increased to a maximum spacing of 0.5 m (toward the end of the 10 m length flume).

III. COMPUTATIONAL METHOD AND SETUP

A. Numerical framework

The governing equations for unsteady, incompressible, viscous flows are the spatially filtered Navier-Stokes equations, which are solved in a Eulerian coordinate system using the in-house large-eddy simulation code Hydro3D,^{30,31} and are as follows:

$$\frac{\partial u_i}{\partial x_i} = 0, \quad (1)$$

$$\frac{\partial u_i}{\partial t} + \frac{\partial u_i u_j}{\partial x_j} = -\frac{\partial p}{\partial x_i} + \nu \frac{\partial^2 u_i}{\partial x_j \partial x_j} - \frac{\partial \tau_{ij}}{\partial x_j} + f_i, \quad (2)$$

where u_i and x_i (i or $j = 1, 2, 3$) are the filtered fluid velocity and position in the three coordinates of space, p denotes the filtered pressure, and ν is the fluid kinematic viscosity. The sub-grid scale stress tensor, τ_{ij} , is approximated using the Smagorinsky sub-grid scale (SGS) model³² considering a filter size equal to the grid size, i.e., $\Delta = (\Delta x \cdot \Delta y \cdot \Delta z)^{1/3}$, which was successfully applied for surface-mounted cylinder flows,

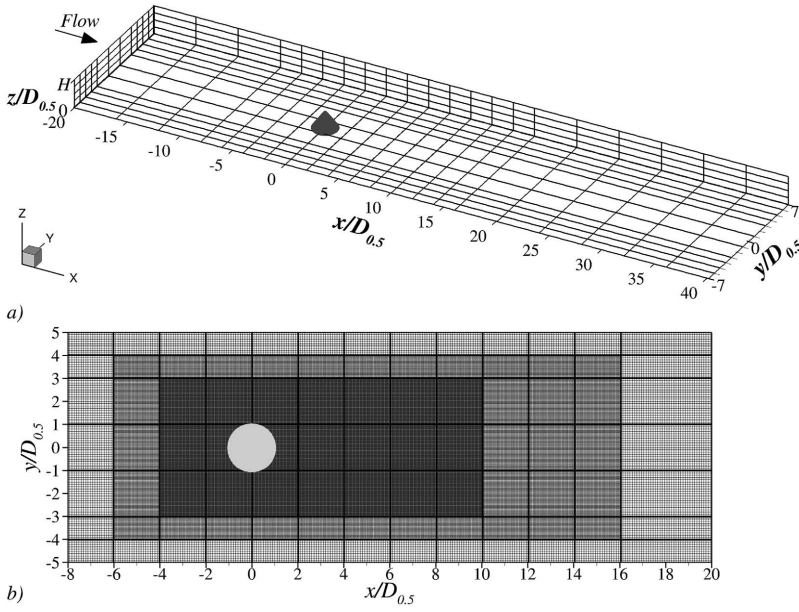


FIG. 2. (a) Sketch of the computational domain where solid lines represent the pattern used for the domain decomposition, and (b) shows a zoom-in view of the locally refined mesh close to the cone.

e.g., Krajnovic.¹⁹ The source term f_i takes into account the external forces derived from the direct forcing Immersed Boundary (IB) method³³ used to represent the obstacle geometry.

The governing equations are discretised using a fourth-order central differencing scheme with a staggered storage of the velocity components on a rectangular Cartesian grid. The fractional-step method is used with a three-step Runge-Kutta predictor to approximate convective and diffusive terms.³⁴ The solution of a Poisson pressure-correction equation using a multi-grid method is adopted as a corrector at the final step. Hydro3D has been validated in a series of hydro-environmental engineering related problems, such as the flow in compound channels³⁵ and tidal steam turbines.³⁶ Recent implementations include an immersed boundary method³⁷ and a Lagrangian particle tracking algorithm for multi-phase flow simulations.^{38,39} Hydro3D is parallelised with a Message Passing Interface (MPI) and uses a domain decomposition technique to divide the computational domain into rectangular blocks [see Fig. 2(b)], which runs on multiple processors. Additionally, it also features a local mesh refinement method⁴⁰ that permits to use fine mesh resolution in areas of interest within the computational domain, e.g., embedding an internal boundary, while using a coarser resolution away from these areas.

The hydrodynamic lift and drag coefficients of the analyzed conical structure are determined from the immersed boundary method forces³⁶ as

$$C_D = \frac{F_x}{1/2\rho AU_0^2}, \quad (3)$$

$$C_L = \frac{F_y}{1/2\rho AU_0^2}, \quad (4)$$

where A is the cone's projected area ($= 1/2HD$, where H is the cone's height and D is the cone's base diameter), ρ is the fluid density, and F_x and F_y are the hydrodynamic forces on the cone in the x - and y -directions, respectively.

B. Computational setup

The computational domain is presented in Fig. 2(a) featuring $60D_{0.5}$ and $14D_{0.5}$ in the x - and y -directions, respectively, replicating the dimensions of the flume. The grid in the vertical direction was set according to the corresponding water depth (H) for each case. The cone was placed at $20D_{0.5}$ from the inlet. Three flow depths were considered to replicate the two submergences: Surface-Piercing (SP) and Shallow-Submergence (SS) from the experimental investigation and a new submergence condition referred to hereafter as Deep Submergence (DS). For the latter case, the flow rate was increased to reproduce a similar mean area velocity as in the other two flow cases. Details of the flow characteristics for these cases are presented in Table I.

A Dirichlet condition was used for the upstream inlet and set to the bulk velocity U_0 used in the experiments (see Table I). A convective condition was employed at the outlet, and no-slip conditions were imposed on the bottom and side walls. The cone boundary was represented using the immersed boundary method that enforces the no-slip condition along the cone's geometry.³³ A frictionless rigid lid condition was employed for the water surface since the Froude number [$Fr = U_0(gH)^{-0.5}$, where g indicates gravity acceleration] for the cases examined was less than 0.1, indicating that the influence of free-surface effects can be deemed small.³⁰

Simulations ran for a total of 250 s (about 7.5 flow-through times), and flow statistics were collected over the last 180 s, similar to the experimental sampling time. Considering that

TABLE II. Grid resolutions used for the mesh convergence.

Mesh	Resolution	$\Delta x = \Delta y(m)$	$\Delta z(m)$
1	Coarse	0.002025	0.00125
2	Medium	0.001016	0.00125
3	Fine	0.001016	0.00075

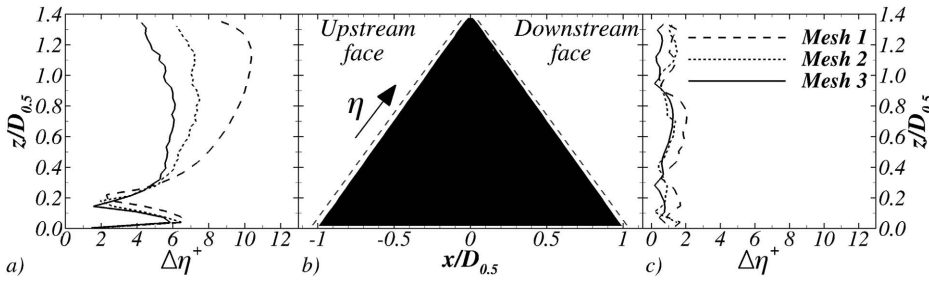


FIG. 3. Values of the cell size in wall-units along adjacent segments in the (a) stoss and (c) lee sides of the cone represented with dashed lines in (b) for the SP case.

the eddy turn-over time ($t_e = H/U_0$) is approximately 1 s, this timeframe is sufficient to obtain reasonably accurate time-averaged values. A Courant-Friedrichs-Lewy (CFL) condition of 0.8 was adopted to ensure numerical stability, which yielded into an averaged time step of $dt^* = dt \cdot U_0/D_{0.5} = 5.7 \cdot 10^{-3}$, $4.1 \cdot 10^{-3}$, and $2.5 \cdot 10^{-3}$ for the coarse, medium, and fine mesh resolutions adopted in the spatial sensitivity study, respectively. Details of the computational meshes are summarised in Table II.

The computational mesh was refined using three levels of local mesh refinement, as shown in Fig. 2(b), with the finest grid resolution distributed around the location of the cone ($-4 < x/D_{0.5} < 10$, $-3 < y/D_{0.5} < 3$, $0 < z/D_{0.5} < H$). Sensitivity to mesh resolution was studied for the SP and SS cases using three different grid resolutions (see Table II). The computational domain was split into 462, 693, and 924 sub-domains for the SP, SS, and DS cases, respectively, which were run using the following number of processors: 76, 114, and 152, respectively, using Supercomputing Wales facilities. The finest grid resolution (Mesh 3) comprised $16, 21$, and 32×10^6 grid points for the SP, SS, and DS cases, respectively. The values of the mesh resolution in wall-units were calculated in segments along the adjacent upstream and downstream segments of the cone at $y/D_{0.5} = 0$, as depicted in Fig. 3(b). Wall-adjacent cell values are given by

$$\Delta\eta^+ = \Delta\eta \cdot u^*/\nu, \quad (5)$$

where the friction velocity, u^* , is given by

$$u^* = (\nu \cdot u_\eta/\Delta\eta)^{0.5}, \quad (6)$$

where u_η is the tangential component of the velocity along the adjacent wall direction obtained from projecting the time-averaged Cartesian velocities on the cone segment, which has a slope angle of 55° . Figure 3(a) shows that along the upstream side the maximum value of $\Delta\eta^+$ is approximately 10.5 for Mesh 1, while the maximum value grid resolution in wall units is 6 for Mesh 3. The upstream side of the cone faces the incident flow, whereas the downstream side is influenced by the low-velocity recirculation region, along which a maximum value of $\Delta\eta^+$ was lower than 2 for all meshes. These values are lower than 11⁴¹ confirming that the no-slip condition along the cone's wall is well accomplished using the immersed boundary method.

IV. RESULTS AND DISCUSSION

The LES results for the surface piercing (SP) and shallow submergence (SS) cases are initially compared and

validated against the experimental data for the time-averaged flow properties. The fundamental differences of the enclosed near-wake and the transition to the far-wake are outlined for each case. The computed instantaneous flow field for each case is subsequently used to identify the dominating turbulent flow structures around the cone and in the downstream wake. To examine the effect of a deeper submergence on wake development, the flow pattern and turbulent structures, LES results are then presented for the deeper submergence (DS). Strouhal and hydrodynamic coefficients are presented to allow key differences in the von Karman shedding pattern to be characterised. Finally a summary of the pertinent flow structures developed under a fully submerged condition is presented. Quantities throughout are normalised using the mean area velocity (U_0) and the conical island's diameter at mid-height ($D_{0.5}$), and the square brackets $\langle \cdot \rangle$ indicate time-averaging.

A. Mesh sensitivity

Three grid resolutions were tested for the SP case to examine grid resolution convergence, and details are presented in Table II. Figure 4 shows vertical profiles of normalised time-averaged streamwise ($\langle u \rangle / U_0$) and vertical ($\langle w \rangle / U_0$) velocities along the plane of symmetry (POS), i.e., at $y/D_{0.5} = 0.0$, at different longitudinal distances downstream from the cone's centre. The accuracy of the LES results improves with increasing grid refinement with the finest mesh resolution (Mesh 3) providing a better agreement with the experimental profiles at $x/D_{0.5} = 1.2$ and 2.5 in terms of time-averaged velocity distribution and magnitudes compared to the coarser meshes. The vertical profile at $x/D_{0.5} = 2.5$ coincides with the transition from the recirculating cell to the far-wake (explained later in Sec. IV B), which poses great complexity and challenges the computational approach, thus corresponds to the larger differences between experimental and numerical results.

Further downstream, LES improves the prediction of the streamwise velocities with increasing distance from the cone at $x/D_{0.5} = 4.3$ and 7.4 . A very good agreement with the vertical velocity magnitudes is also achieved at these verticals indicating that wake recovery is well predicted. Mesh sensitivity testing was also carried out for the SS case; however, the results for the SP case are shown here for brevity. For the SS case, the finest mesh also provided good agreement with the experimental data and this further corroborates that Mesh 3 is sufficiently fine to provide an accurate representation of the flow field for the simulated cases.

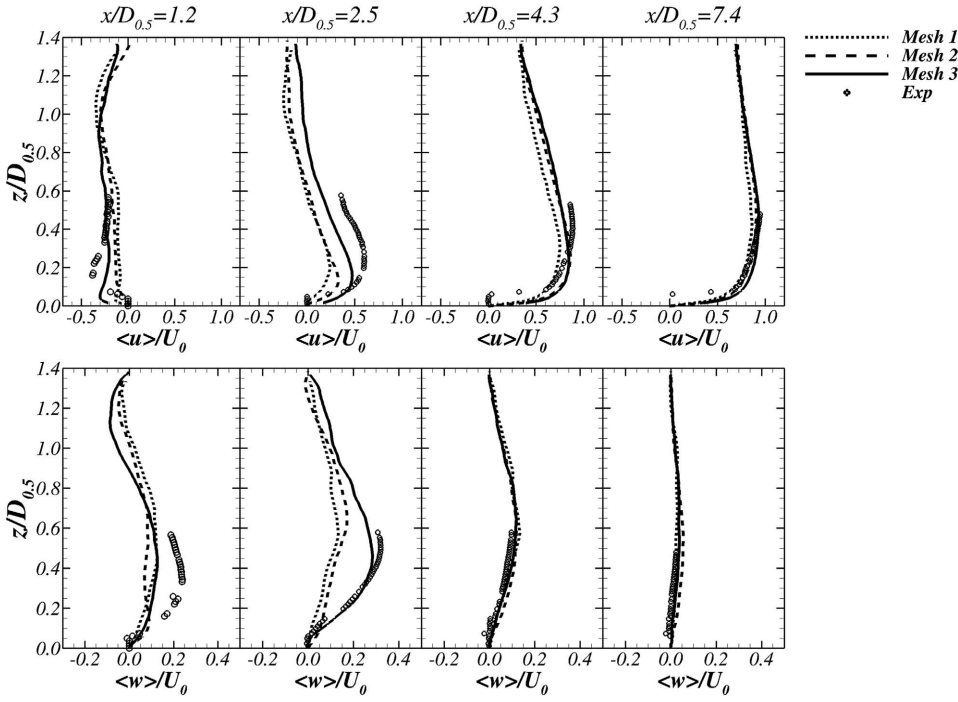


FIG. 4. Profiles of time-averaged streamwise, $\langle u \rangle / U_0$, and vertical, $\langle w \rangle / U_0$, velocities for the SP case using three mesh resolutions.

B. Time-averaged velocity field

The mean velocity field resulting from the flow around the cone is presented in Fig. 5, which presents the experimental (top) and LES (bottom) streamwise velocity contours and flow streamlines for the surface-piercing (SP) and shallow submergence (SS) cases. For both cases, the approaching flow is deflected shortly before the cone. Above a height of $z/D_{0.5} = 0.3$, the flow moves upwards along the inclined face of the cone, while below this height there is a downward flow deflection that is responsible for generating the horseshoe vortex which is described in more detail later.

The flow field development behind the cone is dependent on the submergence level. For the emergent (SP) case, the longitudinal extent of the longitudinal recirculation region is greatest at the cone's tip (almost until $x/D_{0.5} = 3.0$) and steadily decreases toward its base. This is in contrast to the shallow submergence (SS) case where the longitudinal extent of the recirculation region is shortest at the cone's tip, with the extent progressively increasing deeper into the water column until a downstream distance of $x/D_{0.5} = 2.8$ at a height of $z/D_{0.5} = 1.0$.

With the cone piercing the water surface (SP case), the recirculation pattern exhibits two recirculation cores, both attached to the cone's leeward face, with one counterclockwise core located at $z/D_{0.5} = 0.4$ and another immediately downstream of the cone's tip with a clockwise rotation closer to the water surface [see Fig. 5(b)]. These features are well distinguished from the LES results; however, they are not evident in the experimental data. This is not surprising as the ADV is unable to measure the flow field within 10 mm of solid boundaries.

In the SS case, the distribution of the low-velocity region, indicative of the recirculation region immediately behind the

cone (shown in blue), is impacted by the presence of the flow moving between the free-surface layer and over the cone's tip. Such overtopping flow changes the recirculation region pattern when compared to the SP case, which results in a strong upward motion (immediately behind the island) accompanied by a downwash flow downstream from the lee side of the cone. This flow motion induces the enclosed wake to feature a clockwise rotation that is well indicated by the streamlines in Figs. 5(c) and 5(d). LES predicts the presence of the core of the horizontal recirculation at approximately $z/D_{0.5} = 1.2$; this is further downstream than the recirculation core observed in the SP case that was near the cone's surface. The horizontal roller is located slightly below the level of the cone's tip, which is in line with the experimental results [see Figs. 5(c) and 5(d)]. The presence of a horizontal roller for the submerged cone has also been observed for the submerged cylinder, cuboid and ellipsoid flow.^{1,11,17,21,42} This upward flow region is significantly greater compared to that observed in the cylinder flow^{1,21} due to the cone's geometry and inclined leeward face.

For both SP and SS cases, the downstream distance at which the recirculation region is contained and the flow reattaches to the overlying current is slightly longer for the LES compared to the experimental measurements. At the bed, the reattachment length predicted by the LES is located at $x/D_{0.5} = 2.2$ and 2.5 for the SP and SS cases, respectively, while it is located at $x/D_{0.5} = 1.8$ and 1.9 , respectively, for the experimental data. Note the similar pattern of the recirculation area, and slight overestimation of the enclosed wake length of the LES compared to experiments was obtained by Palau-Salvador *et al.*¹¹ and Afgan *et al.*²⁵ in the LES of the flow around submerged cylinders. Immediately downstream of the recirculation region, i.e., far-wake region, the flow distribution predicted by the LES reproduces well the experimental results

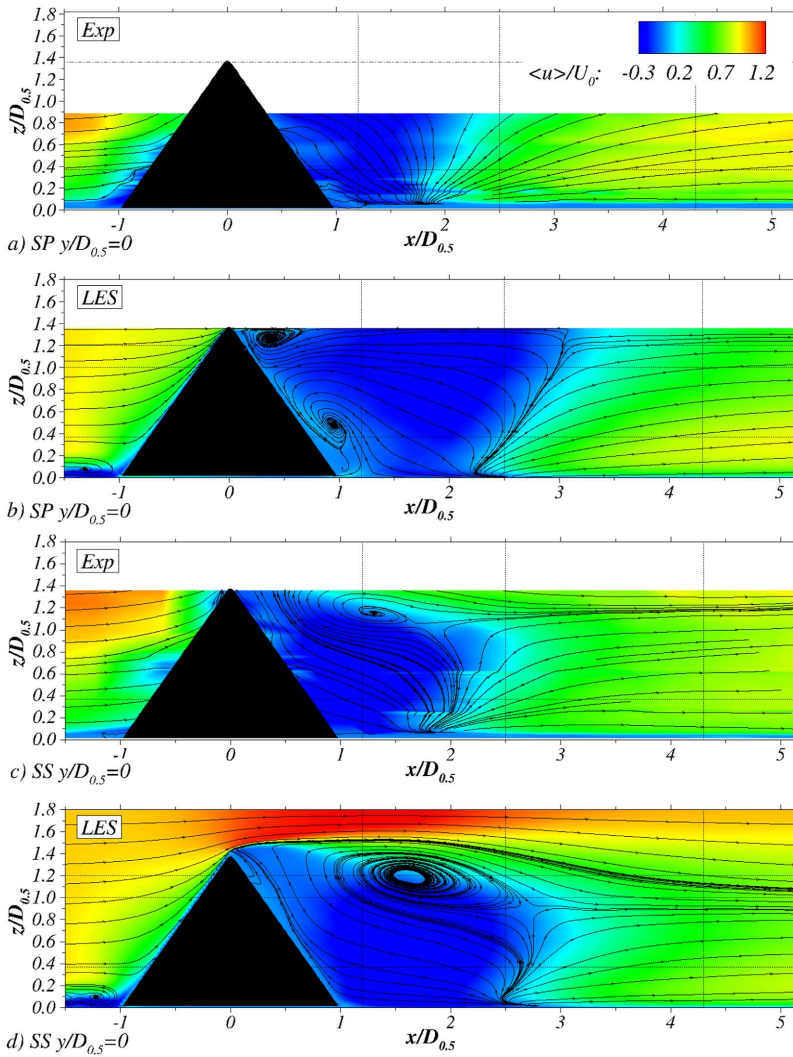


FIG. 5. Transversal planes at $y/D_{0.5} = 0$ with contours of normalised streamwise velocities for the SP [(a) and (b)] and SS [(c) and (d)] cases. Comparison between experimental and LES results.

as confirmed from the vertical profiles of velocities shown in Fig. 4. Differences between the SP and SS cases are also indicated in the magnitude of the velocity reversal along the channel bottom between the cone's base ($x/D_{0.5} = 1.0$) and the closure of the separation region ($x/D_{0.5} = 2.2-2.5$) with the minimum time-averaged streamwise velocity of $-0.35U_0$ and $-0.15U_0$ for the SS and SP cases, respectively. Such differences indicate that the flow reversal is stronger in the SS case.

The development of the enclosed wake over the water column is observed by comparing the contours of streamwise velocities at different elevations, i.e., $z/D_{0.5} = 0.37, 1.0, 1.2$, as shown in Fig. 6. For the SS case, the transverse extent of the recirculation region decreases with elevation which is as wide as the cone base at $z/D_{0.5} = 0.37$ [see Fig. 6(b)]. At an elevation of $z/D_{0.5} = 1.0$, the transverse extent of the wake is at its maximum, and with increasing elevation, it decreases in size and strength (see Figs. 5 and 6). The overlying flow in the shallow submergence case reduces the vertical extension of the recirculation region and dampens the strength of the reverse flow at the cone's tip [see Fig. 6(f)], and hence the recirculation cell is no longer present at the highest elevation ($z/D_{0.5} = 1.2$). While for the SP case, the low-momentum region continuously

grows in longitudinal extent with increasing elevation as the loci of the recirculation cores move further downstream. This is also observed close to the cone's tip, where the diameter and thus the blockage ratio are smaller. Afgan *et al.*²⁵ presented a similar wake pattern in the flow around a submerged cylinder.

The largest difference between SP and SS cases is found at $z/D_{0.5} = 1.2$, as in the former case the flow is notably deflected and recirculates downstream, while in the SS case there is almost no recirculation due to the dampening and downwash of the overlying flow. At the plane closest to the channel bed, the length of the recirculation zone is slightly longer for the shallow submergence (SS) case compared to the emergent (SP) case, as observed from both the experiments and the LES. In both cases, in terms of the strength of the velocity reversal and width of the wake, there is satisfactory good agreement between the LES and experimental results. Furthermore, the velocity recovery occurs at a similar downstream distance ($x/D_{0.5} > 3$).

The distribution of vertical velocities at the same z -planes is presented in Fig. 7. For the two submergence cases, at $z/D_{0.5} = 0.37$, the areas of low streamwise velocity, indicated by the blue regions in Figs. 6(a) and 6(b), coincide

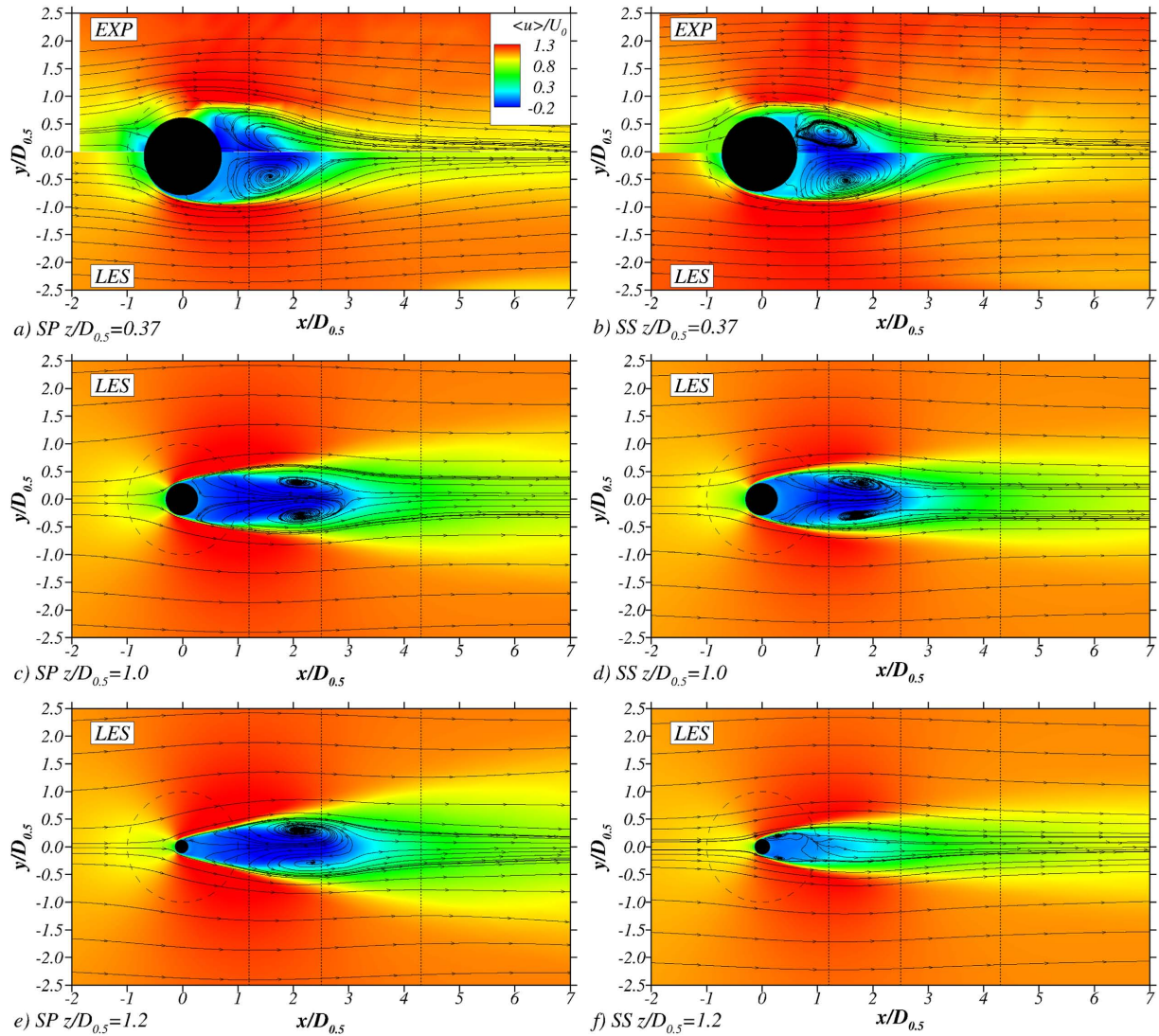


FIG. 6. Normalised streamwise velocities for the SP (left) and SS (right) cases at $z/D_{0.5} = 0.37$ (top), 1.0 (middle), and 1.2 (bottom). In the top plots, the upper half is for the experimental data and the lower half is for the LES results.

with the areas of the highest upward velocities, as indicated by the red regions in Figs. 7(a) and 7(b). At $z/D_{0.5} = 1.0$, the presence of the overtopping flow layer in the SS case generates the downward movement of the flow immediately downstream of the horizontal recirculation cells, which is accompanied by an upward movement of the flow immediately on the lee side of the cone's face [Fig. 7(d)]. This velocity pattern coincides with the clockwise recirculation of the near-wake observed in Fig. 5. On the contrary, Fig. 7(c) shows that in the SP case there is a downwash flow along the borders of the recirculation area with a small upward vertical velocity shortly after the recirculating cells. Closer to the water surface, at $z/D_{0.5} = 1.2$, a small upward movement of the flow is observed for the SP case on the lee side on the cone, whereas a much larger upward flow region persists throughout the water column for the SS case [Figs. 7(e) and 7(f)].

The varying diameter of the cone over its height induces the downstream wake to feature a recirculation cell as shown in Fig. 5, which is more three-dimensional in nature than that

generated in the flow around cylinders.^{1,11} Figure 8 presents time-averaged streamwise velocity contours and flow streamlines at different cross sections in the downstream direction ($x/D_{0.5} = 1.2, 2.5$, and 4.3). According to Fig. 5, the cross section at $x/D_{0.5} = 1.2$ slices through the recirculation area, while $x/D_{0.5} = 2.5$ is located in the recirculation region close to its downstream extent very close to the reattachment point, and $x/D_{0.5} = 4.3$ is downstream of the recirculation region. At $x/D_{0.5} = 1.2$, two counter-rotating vortices are generated behind the cone as the free-stream side flow is entrained into the low-momentum wake, and this is present for both SP and SS cases.¹ Streamlines indicate that at the centre of the flume ($y/D_{0.5} = 0$), the flow travels upwards for both submergence levels as previously indicated from the vertical velocities in Fig. 7.

Figures 8(a) and 8(b) show that regardless of whether the cone is emergent (pierces through the water surface) or submerged (the cone's apex is below the water surface) the LES predicts two cells in the laterals of the cone near the channel bed between $y/D_{0.5} = 1.5$ and $y/D_{0.5} = 2.5$. These correspond to

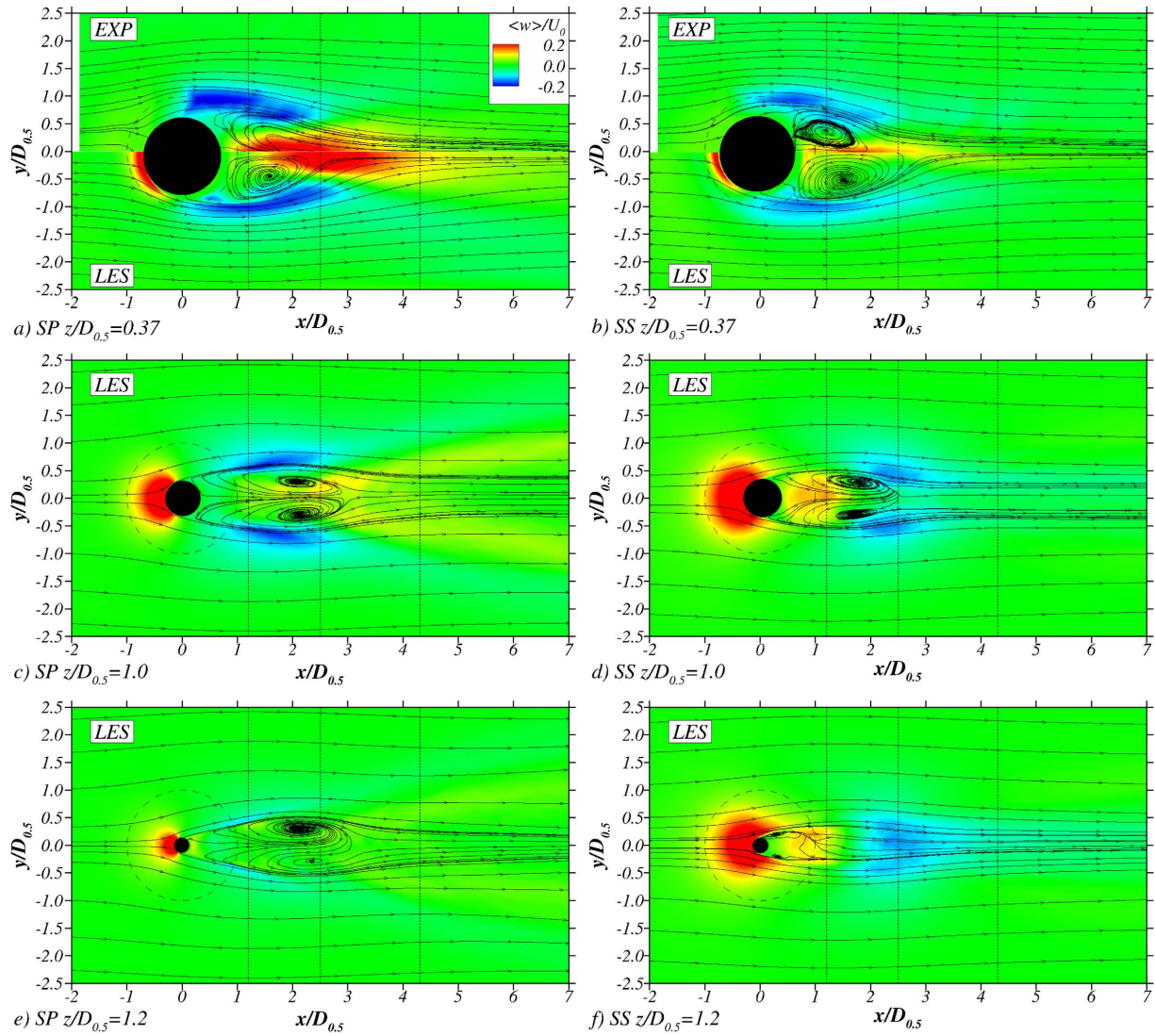


FIG. 7. Normalised vertical velocities for the SP (left) and SS (right) cases at $z/D_{0.5} = 0.37$ (top), 1.0 (middle), and 1.2 (bottom). In the top plots, the upper half is for the experimental data and the lower half is for the LES results.

the horseshoe vortex legs and feature a distinct helical motion. The development of such a double-core horseshoe vortex structure was also appreciated in the transversal planes in Figs. 5(b) and 5(d) with the horseshoe cores situated at $x/D_{0.5} = -1.25$ and $x/D_{0.5} = -1.6$ upstream of the cone. The complexity of the horseshoe vortex has been identified in other studies^{9,19} with the existence of both primary and secondary horseshoe vortices as well as a tertiary one attached to the upstream side of the body and which is not observed in the present study.

At a longitudinal distance $x/D_{0.5} = 2.5$, the velocity reversal in the wake weakens for both cases although the low-momentum region is distributed over the upper half of the water column for the SP case whilst over the lower half for the SS case. It is worth noting that for the submerged case (SS) the streamlines indicate that the flow above an elevation of $z/D_{0.5} = 0.9$ is directed toward the channel bed, while below this elevation the flow moves upwards. This feature in the SS case indicates that its wake is more three-dimensional than in the SP case in which at $x/D_{0.5} = 2.5$ the flow reversal is

only directed toward the free-surface. The experimental results suggest a higher wake recovery rate than LES predictions as the streamwise velocity contours at a longitudinal distance of $x/D_{0.5} = 2.5$ present only positive values. Such differences with the LES predictions agree with the experimental results (see Fig. 4).

Further downstream, at $x/D_{0.5} = 4.3$ (outside the recirculation region), there is a better agreement in the wake signature between the experiments and LES, and the absence of flow reversal for both cases is consistent with Fig. 5. For the SP case, a secondary current is induced from the blockage generated by the cone depicted from the recirculating cell located at a similar elevation to the cone's tip but displaced as a consequence of the flow deflection due to the cone obstruction [Fig. 8(e)]. The flow overtopping present in the SS case neglects the generation of such secondary features in the wake. Recirculating cells near the channel bottom evidence the horseshoe vortices bounding the wake even further downstream of the cone and into the near-wake; this will be detailed in Sec. IV C.

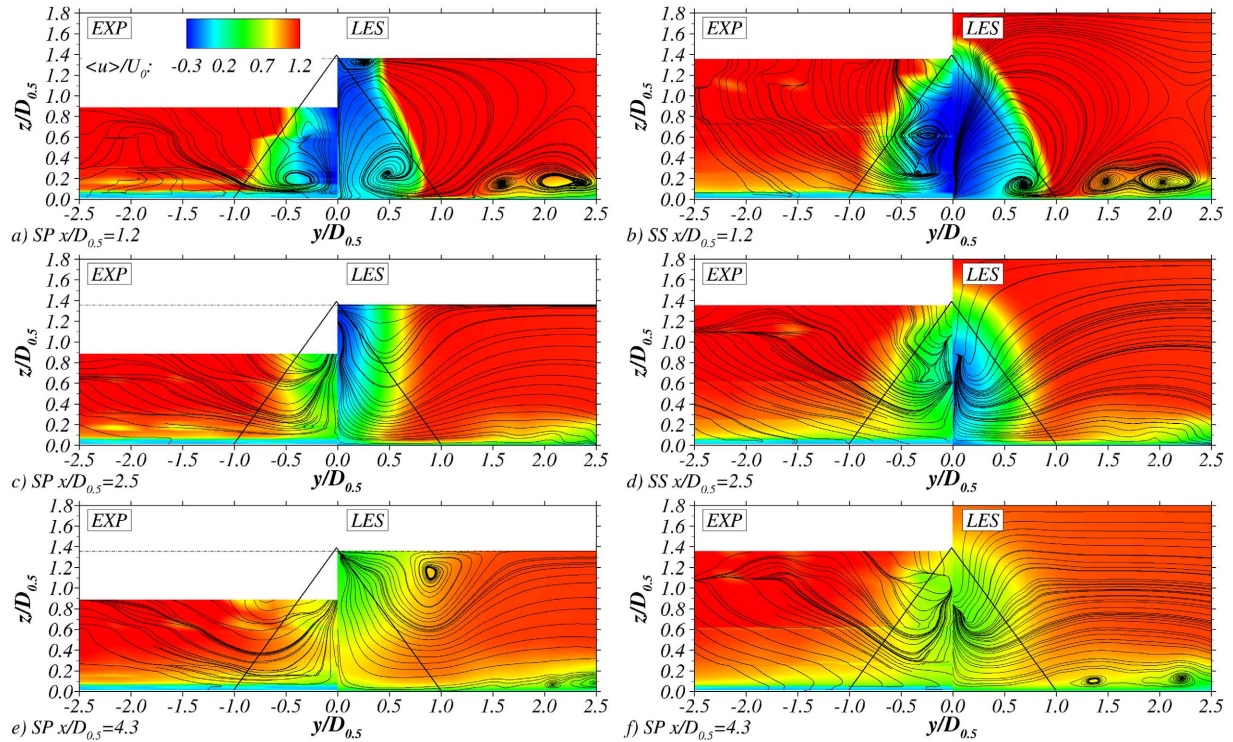


FIG. 8. Contours of normalised mean streamwise velocity in planes normal to the x -axis behind the cone at $x/D_{0.5} = 1.2$ (top), 2.5 (middle), and 4.3 (bottom). The figures in the left hand side column are for the SP case and those in the right hand column are for the SS case. In each individual figure, the left hand side is the experimental data and the right hand side is for the LES results.

C. Instantaneous flow structures

The flow around the cone is highly three-dimensional and is dominated by the presence of both large-scale and small-scale structures whose pattern changes depending on the level of submergence. The main features present in the wake of the SP and SS cases are identified in Fig. 9, which presents a plan-view of the instantaneous flow structures represented with iso-surfaces of z -vorticity ($\omega_z \pm 8$), coloured with water column elevation. For the SP case, there is a blockage throughout the water column and no flow overtopping, and thus the flow is strongly deflected around the cone's sides near its apex as shown in Fig. 9(a). The enclosed wake extends for about two base diameters downstream before large-scale von Karman vortices (KV) start to shed and be transported by the mean flow in the streamwise direction but also laterally.¹¹ This agrees well with the transition from near- to far-wake observed in the time-averaged velocity distribution in Fig. 5. In the SS case, despite the cone's apex being submerged below the water surface, the KV reach the water surface further downstream indicating that the overtopping flow layer constrains the vertical expansion of these energetic flow structures. For the horizontal extension presented in Fig. 9, the SP case exhibits three KV, while only two are observed in the SS case indicating a higher shedding frequency for the former case, as it is discussed later in Sec. IV F.

A Kelvin-Helmholtz instability occurs as the cone's surface shear layers break down developing the large-scale shear-layer vortices (SLV), which are eventually decomposed into smaller scale structures and are analogous to the cylinder flow.⁴³ The generation and shedding of these structures from

the inclined sides of the cone appear to be consistent with both surface-piercing and shallow submergence cases. A horseshoe (HS) vortex is generated near the bed for both cases enclosing the upstream base of the cone and the recirculation region as

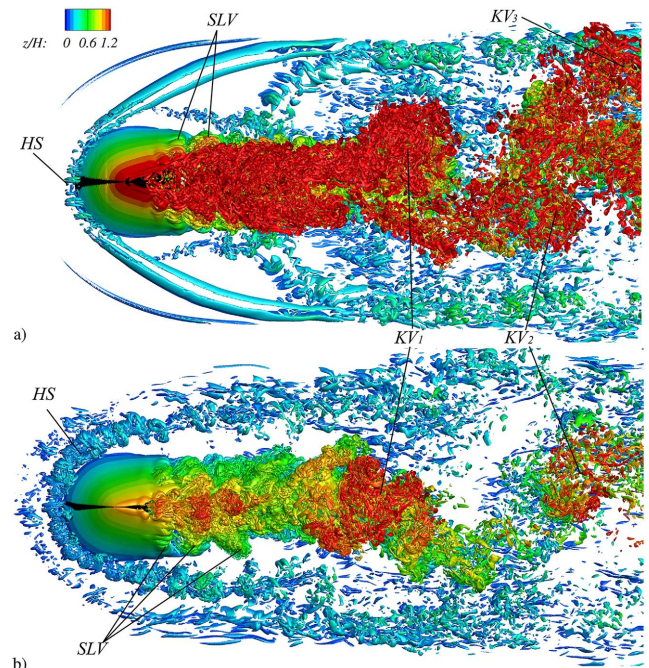


FIG. 9. Top view of the turbulent structures generated in the (a) SP and (b) SS cases represented with vertical vorticity iso-surfaces coloured with values of relative water depth normalised with the cone's height.

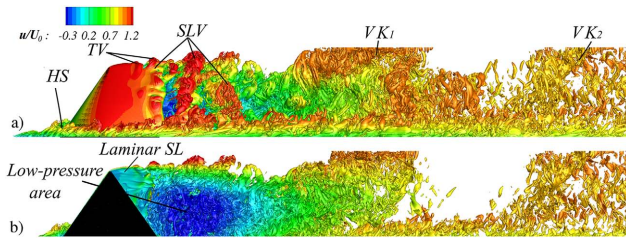


FIG. 10. Side views of the turbulent structures generated in the SS case represented with z -vorticity iso-surfaces coloured with instantaneous streamwise velocity values. (b) shows the side view of iso-surfaces for $y/D_{0.5} > 0$.

previously indicated in Fig. 8. The HS in the SP case features a laminar region in contrast to the SS case in which the HS has a turbulent nature in all its extend. In the surface-piercing case, the legs of the horseshoe vortex closely bound the recirculation region, while for the SS case the legs are splayed outwards. This turbulent structure features a helical motion and wraps around the downstream wake as depicted in Figs. 8(a) and 8(b) but with negligible interaction with the KV, similar to the horseshoe vortex structure developed in cylinder flows, see the work of Sumner.⁴³

Figure 10(a) shows the side view of the instantaneous flow structures for the SS case with the analogous z -vorticity iso-surfaces of Fig. 9 coloured with streamwise velocity values, and Fig. 10(b) shows the flow field for the right hand side of the channel, i.e., $y/D_{0.5} > 0$. The laminar shear layer formed along the sides of the cone is again depicted, and it stays fairly straight in the z -direction until the roll-up SLV structures are observed at a downstream distance which coincides with the cone's base. Figure 10(b) depicts the

laminar-to-turbulent transition of the shear layer which is achieved further longitudinal distance from the cone's apex but closer to its base, which suggests that the flow development near the cone varies over its height. The tip vortices (TV) are clearly depicted by the iso-surfaces in Fig. 10 and combine with the SLV once the shear layer becomes unstable, and they form a unique structure: an arch vortex. The top of the arch is elongated upwards toward the free-surface and tilted in the downstream direction due to the top of the arch being convected at a quicker rate than its vertical sides due to the presence of the higher streamwise velocities located in the surface flow layer as shown in Fig. 5(d). This effect is enhanced by the recirculating motion of the flow in the low-velocity area enclosed behind the cone [Fig. 10(b)] that enlarges the shear in the border of this recirculation region along which the arch vortices are transported. This is in agreement with studies on flow around ellipsoidal bodies, particularly the downstream tilting of arch vortices observed for an ellipsoid when its longer axis is aligned in the spanwise direction.¹⁷ Figure 10(a) shows that the coherence of the arch vortex is lost before the onset of the von Karman vortex shedding and that the horizontal extension of the KV structures is proportional to the diameter of the cone at its basement whilst they are vertically distributed over the whole water depth. Thus, despite the cone's height being lower than the water surface elevation for the SS case, the von Karman vortices expand over the whole water depth constrained by the presence of the free-surface layer.

D. Second-order statistics

Figure 11 presents the distribution of the streamwise velocity fluctuation, $\langle u' \rangle / U_0$, transverse velocity fluctuation,

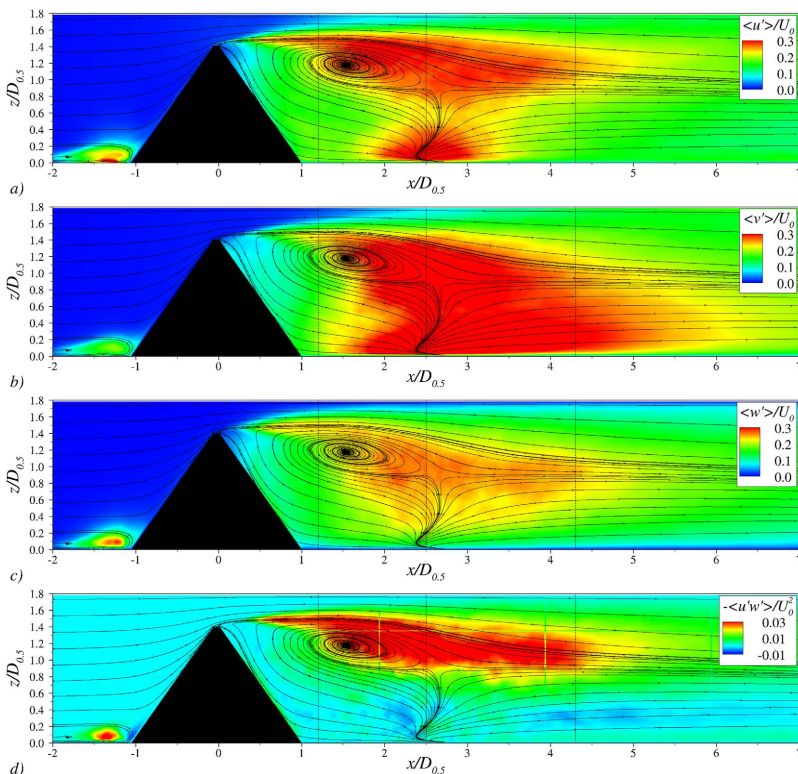


FIG. 11. Transversal planes at $y/D_{0.5} = 0$ for the SS case with contours of normalised (a) streamwise, (b) transversal, and (c) vertical velocity fluctuations and (d) primary Reynolds shear stresses.

$\langle v' \rangle / U_0$, vertical velocity fluctuation, $\langle w' \rangle / U_0$, and normalised primary Reynolds shear stresses, $-\langle u'w' \rangle / U_0^2$, along the longitudinal POS ($y/D_{0.5} = 0.0$) for the SS case. Note that mean velocity fluctuations^{0.5} are denoted as $\langle u'_i \rangle$ for the sake of simplicity. The largest values of normal Reynolds stresses are found along the transition from the recirculating region to the far-wake as this coincides with the area where shear-layer vortices lose coherence due to their interaction with the free-stream flow and recirculating region, and where the large-scale von Karman vortices are generated and shed, as depicted in Fig. 9(b). Downstream of the island's tip at an elevation of $z/D_{0.5} = 1.5$, peak values of velocity fluctuations are also triggered due to the interaction of the tip and shear layer vortices with the overtopping flow (see Fig. 10), and this is more noticeable for the turbulent intensities in the streamwise and vertical directions.

It is worth noting that the large values of transverse velocity fluctuations are distributed in a greater area compared to those in the streamwise direction, i.e., mean flow direction, which is indicative of the alternating and meandering nature of the shedding of the energetic von Karman vortices, as shown in Fig. 9. High values of horizontal and vertical velocity fluctuations are present immediately upstream of the cone's base where the horseshoe vortex is developed. Their unstable nature triggers fluctuations especially in the streamwise and vertical velocities due to its rotation nature as depicted in the streamlines of Fig. 5.

Downstream of the cone, a region of high primary Reynolds shear stress, $-\langle u'w' \rangle$, is located in the upper half of the water column ($z/D_{0.5} > 1.0$), after the recirculation region at $x/D_{0.5} = 1.6$. Here, the incident flow overtops the cone and entrains and interacts with the recirculation region increasing turbulence levels. Time-averaged metrics $\langle u' \rangle$, $\langle w' \rangle$, and $-\langle u'w' \rangle$ decay after $x/D_{0.5} = 4.3$, whereas the transverse velocity fluctuations $\langle v' \rangle$ remain relatively large until a downstream distance of approximately $x/D_{0.5} = 6$ due to the von Karman vortex shedding. This corresponds to the downstream distance at which the von Karman vortex loses coherence [see Figs. 9(b) and 10]. The distribution of primary Reynolds stresses for the SP case exhibits a different pattern (contours not shown here) as their maximum values are mostly concentrated along the transition between the recirculating bubble and the far-wake. For the SP case, the transverse velocity fluctuations are again significant and similar in magnitude to that of the streamwise velocity fluctuations.

E. Deeper submergence case

The impact of a deeper submergence (DS case) on the wake was also examined using the LES. The flow depth was increased to $H = 0.22m$ corresponding to a relative submergence of $H/h = 1.92$, while the same mean area velocity as in the surface-piercing case was adopted (see Table I for details). The main changes in the developed mean streamwise velocity field are observed in the contours of mean streamwise velocities along the POS as shown in Fig. 12. The low-pressure area behind the structure is similar to that found for the SS case [see Fig. 5(d)] with a similar location of the recirculating cell core (at $x/D_{0.5} = 1.5$ and $z/D_{0.5} = 1.2$). The increase in the flow depth allows a greater

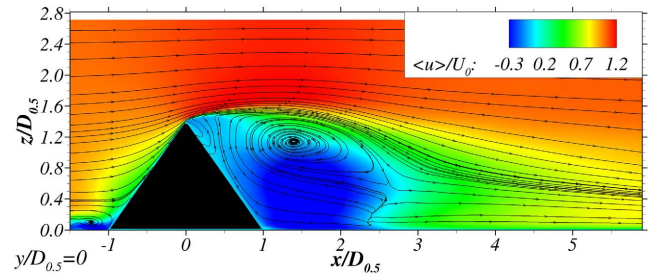


FIG. 12. Flow streamlines and contours of mean streamwise velocity at the channel centre plane $y/D_{0.5} = 0$ for the DS case.

proportion of the water column to overtop the cone, which reduces the blockage effect of the island with flow reattaching at a slightly quicker rate downstream (at $x/D_{0.5} = 2.5$ near the channel bed) than for the SS case. Such similar properties of the recirculation region when the cone is completely submerged can be expected given their similar Froude number of $Fr \approx 0.068$. A shortened recirculation length with increasing submergence has also been observed for cylinder flows in an experimental study.²¹

A comparison of the instantaneous flow generated behind the cone for the three submergence cases is presented in Fig. 13, with a plan view contour plots of instantaneous vertical vorticity ($\omega_z \pm 5$) at three different elevations: $z/D_{0.5} = 0.5, 1.0$ and 1.3 . For the three cases, the instantaneous wake development is different depending on the position in the water column as the cone's diameter and the local Reynolds number based on the cone's diameter decrease with increasing elevation, in accordance with studies conducted on flow around circular cylinders at different Reynolds numbers.^{2,7} In the plane at $z/D_{0.5} = 0.5$, there are small structures coming from the horseshoe vortex which seems to interact with the large-scale von Karman vortices in the three cases, similar to the experimental visualisations in the flow around a circular cylinder from the work of Palau-Salvador *et al.*¹¹ For the emergent case (SP), the onset of vortex shedding commences earlier than for the submerged cases (SS and DS), i.e., the length of the enclosed wake is shorter, and for all the cases, this is followed by a well-defined von Karman vortex street. The spanwise vorticity contours also indicate that for the SP case the shedding frequency of these vortices is higher than for the submerged cases due to the larger blockage effect of the cone.

Wakes developed behind the cone for the SS and DS cases exhibit a similar nature with the largest differences observed for the plane closest to the cone's tip at $z/D_{0.5} = 1.3$ [see Figs. 13(h) and 13(i)]. In the SS case, the enclosed wake is directly followed by the vortex shedding, whereas for the DS case these are somehow discontinuous at this elevation in the water depth. It is worth noting that for the deeply submerged case, the larger flow overtopping (Fig. 12) induces a lower constraint of the free-surface on the von Karman vortices which in turn allows them to be detached from the enclosed wake at $z/D_{0.5} = 1.3$.

A three-dimensional view of the flow structures developed in the DS case is presented in Fig. 14 with iso-surfaces of z -vorticity in which the same flow features than for the SS

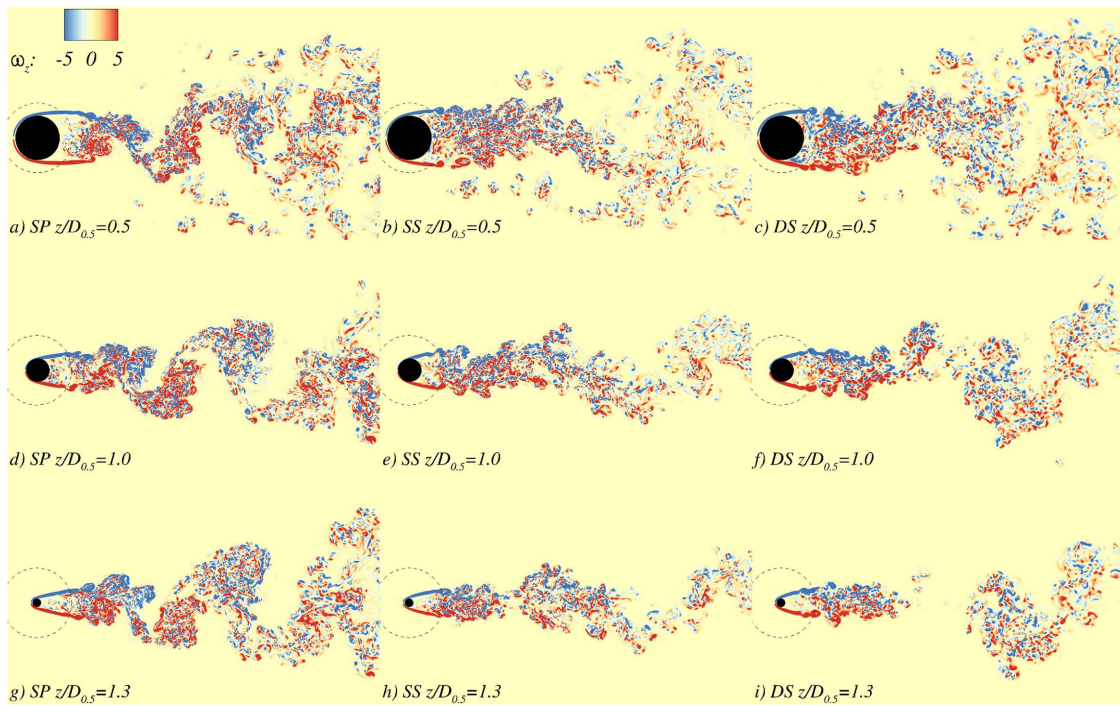


FIG. 13. Contours of instantaneous vertical vorticity (ω_z) for the SP (left), SS (centre), and DS (right) cases at three z -planes at heights of $z/D_{0.5} = 0.5$ (top), 1.0 (middle), and 1.3 (bottom). Dashed line indicates the cone's basement perimeter.

presented in Figs. 9(b) and 10 are observed. The tip vortices are again identified from Fig. 14, and these combine with the shear layer breakdown vortices to generate the so-called arch vortices. Similar to the SS case, for the DS case, the arch vortices are tilted in the downstream direction as they meet the high-velocity area over the cone which induces a faster motion at the arch top than at the arch's vertical legs. The higher submergence of the cone in the DS case reduces the strong vertical shear in the border of the recirculating region encountered in the SS case that induced the arch vortices being convected upwards toward the water surface. The latter effect is not observed for the DS case although in these flow conditions arch vortices are more tilted in the downstream direction than for the SS case [see Figs. 14 and 10(a)]. The ability of the arch

vortices in the DS case to impinge toward the recirculation area shortly downstream compared to their upward motion in the SS case can be observed in Figs. 13(h) and 13(i) with a discontinuity in the shed structures downstream the cone's apex for the deeper case. The energetic von Karman vortices are also present in the wake behind the cone for the DS case, but they lost coherence at the captured instant in time and thus difficult to depict from Figs. 14 and 17.

In view of the present results, the key flow structures in the wake of a submerged conical island are proposed in Fig. 15. These structures include (a) the formation of the horseshoe vortex at the upstream junction between the cone's base and channel bed, which bounds the recirculation region, (b) the breakdown of the large-scale shear layer vortices from the

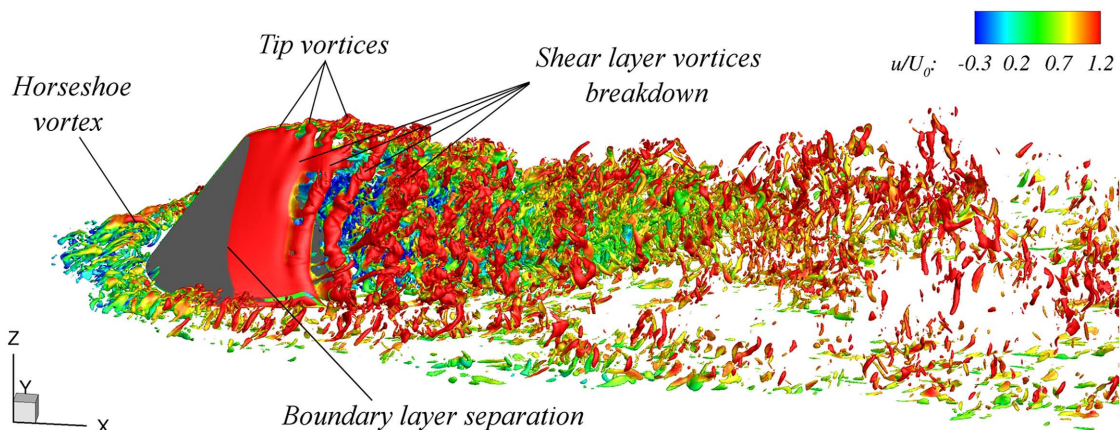


FIG. 14. Turbulent structures generated in the flow around the cone for the DS case using iso-surfaces of instantaneous vertical vorticity coloured with normalised instantaneous streamwise velocity values.

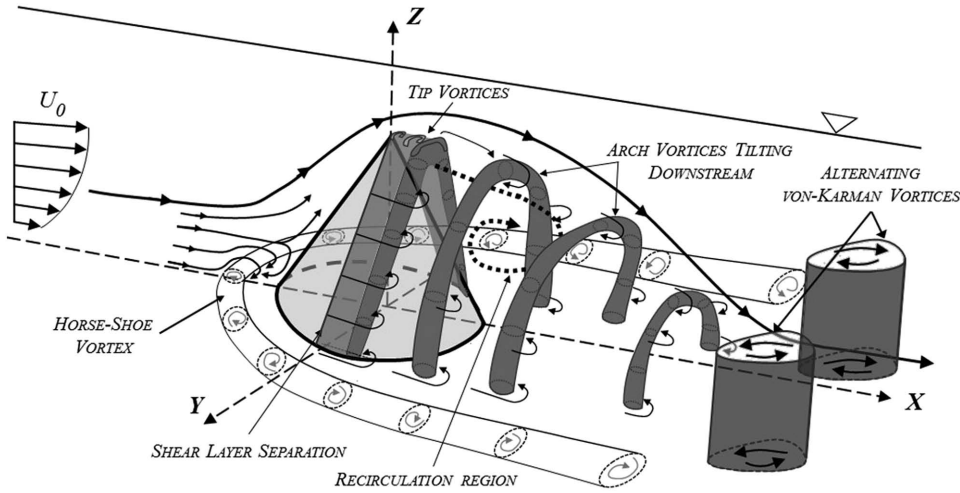


FIG. 15. Proposed schematic of the flow structures generated in the flow around a submerged conical island.

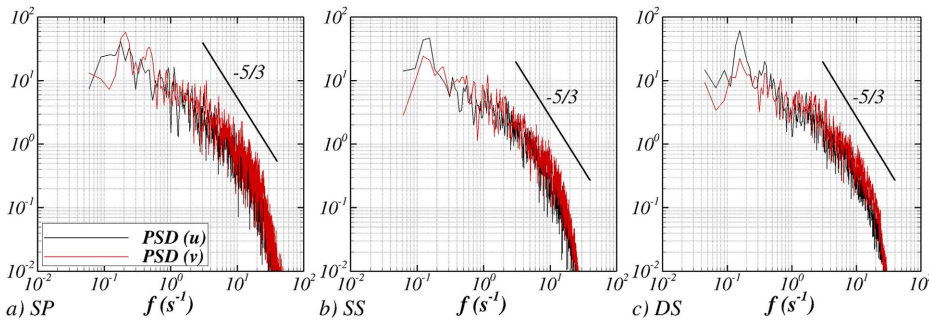


FIG. 16. Power Spectral Density (PSD) of u - and v -velocities obtained from the time series in a point located at $x/D_{0.5} = 8.5$, $y/D_{0.5} = 0.75$, and $z/D_{0.5} = 1.0$ for the (a) SP, (b) SS, and (c) DS cases.

sides of the cone into smaller scale structures, (c) the formation of tip vortices from the apex of the cone, and (d) the presence of arch vortices before the onset of (e) alternating shedding of the energetic von Karman vortices. The arch vortices are tilted in the downstream direction, a short distance downstream of the cone, and for the lower submergence case (SS) elongated upwards toward the water surface due to the stronger vertical shear layer associated with the shallower submergence.

F. Hydrodynamic forces and far-wake characterisation

The wake structure observed for all three cases in Fig. 13 consists of an enclosed recirculation region followed by a von Karman vortex street whose shedding frequency is dependent on the cone's submergence level. The frequency values are determined from the Power Spectral Density (PSD) presented in Fig. 16 obtained from the streamwise (u) and transversal (v) velocity time series at a point in the shedding path ($x/D_{0.5} = 8.5$, $y/D_{0.5} = 0.75$, $z/D_{0.5} = 1.0$). The energy peaks from the spectra indicate that the low-frequency structures dominate the flow and the frequency of the energy peaks, f_p , identifies the shedding frequency of such structures, and these are summarised in Table III together with the Strouhal number ($St = f_p D_{0.5} / U_0$). The surface-piercing case features the highest Strouhal number ($St = 0.239$) as a result of its shallower flow depth and greater blockage effect and with a value almost double from that obtained for the DS case ($St = 0.128$). The two submergence cases have very similar Strouhal number values as would be expected, given the commonality of their vortex shedding patterns (Fig. 13). Such an

increase in the vortex shedding frequency in the SP case compared to the other cases is expected, given the differences in the vortex shedding patterns [see Figs. 13 and 9(a)], and it exemplifies the constraining effect of the overtopping flow on the von Karman shedding. Note that the values of St for the submerged cases (SS and DS) are very similar to those determined for submerged cylinders.^{5,8}

The high energetic peaks found in the production range of the energy spectra confirm the appropriateness of the computational setup to capture the dominant flow structures. The energy cascade along the inertial subrange of the velocity spectra features the $-5/3$ Kolmogorov law, as observed for frequencies between 3 and 10. Since this frequency the dissipation rate increases due to the action of the SGS model.⁴⁴ Overall the range of resolved frequency expands for more than two decades indicating that the adopted grid resolution is adequate.¹¹

Table III presents details of the time-averaged drag coefficient [C_D , Eq. (3)] and root-mean-square (rms) of the lift coefficient [C_L , Eq. (4)] obtained from the hydrodynamic forces on the cone. The drag coefficient is greatest for the

TABLE III. Hydrodynamic characteristics of the forces in the conical island: SP surface piercing, SS slightly submerged, and DS deeply submerged.

Case	f_b (s^{-1})	St	Mean C_D	rms C_L
SP	0.295	0.239	1.108	0.0585
SS	0.142	0.146	0.882	0.0620
DS	0.158	0.128	0.826	0.0807

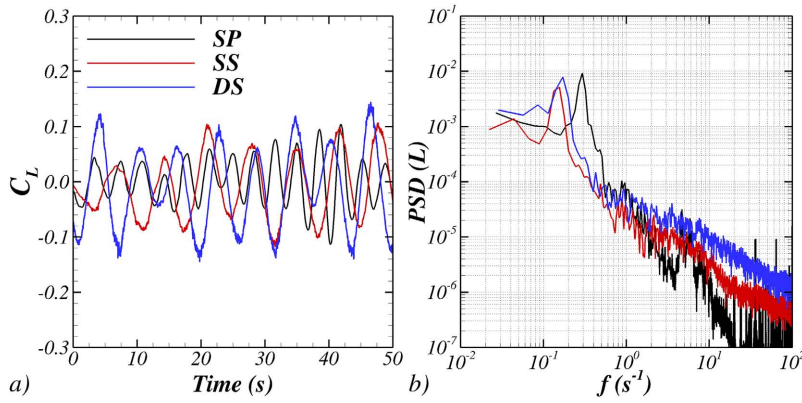


FIG. 17. Comparison of (a) time history of the lift coefficient (C_L) for the first 50 s since the start of the velocities time-averaging and (b) power spectral density of lift force (L) for the three cases.

emergent case with a value of 1.108 and a minimum when the cone submergence is the greatest, i.e., in the DS case, where the mean C_d value is 0.826. On the contrary, for the DS case, the *rms* of C_L is the largest among the analyzed cases indicating that vortices induce a larger transversal force oscillation in the cone.

Figure 17 presents the lift coefficient time series and the corresponding PSD of the lift force for the three cases. The lift force oscillation indicates the alternating lateral forces on the cone due to the vortex shedding. The largest C_L amplitude is achieved for the deepest submergence which is also indicated by its higher root-mean-square lift coefficient value (see Fig. 17 and Table III). In contrast, the SP case presents a C_L time series with a lower amplitude but much higher oscillation frequency than the other cases. Energy peaks from the spectra of lift force indicate that both SS and DS cases present a similar shedding frequency [see Fig. 17(b)], and these coincide with the peak frequency values from the velocity spectra according to Figs. 16(b) and 16(c). Additionally, the energy peak for the DS case is larger than that for the SS case indicating that the energy of the shed vortices is higher for the former case, in keeping with the higher lateral force amplitude as indicated by the higher *rms* C_L value.

Both velocity spectra and lateral force times series suggest that the lower proportion of the flow which is blocked by the cone results in a reduced vortex shedding frequency, a lower drag coefficient, and more lateral force oscillation (Figs. 16 and 17). These results are consistent with studies conducted with infinite and finite cylinders.^{1,12} Additionally, despite the geometrical differences between cylinders and conical structures, the results presented here demonstrate that the wake and hydrodynamic forces are characterised by a single energy peak which is in line with studies conducted with cylinders.¹⁰

V. CONCLUSIONS

Large-eddy simulations (LESs) and experiments have been used to investigate the wake generated by a conical island for three levels of submergence: surface-piercing ($H/h = 0.96$), shallow submergence ($H/h = 1.24$), and deeply submerged ($H/h = 1.92$) conditions. The flow around conical structures is remarkably three-dimensional with a wide range of turbulent scales dominating the flow features that are difficult to characterise and identify from observational and experimental

measurements. Thus, the high-resolution LESs allowed for the identification of key instantaneous flow structures, reproducing well the time-averaged flow properties observed in the experiments. Due to instrument limitations, it was not possible to measure the near-surface velocity field. This served as further motivation for performing the numerical simulations.

The time-averaged velocity contours indicated that the incident flow approaching the cone is deflected laterally and upwards along the cone's upstream face, reaching the recirculation area on the downstream side of the body. In the submerged cases (when there is flow overtopping the cone's apex), the recirculation region is shortened both in its horizontal and vertical extent, whereas the enclosed bubble expands over the whole water depth and further downstream when the cone pierces the water surface. The flow features downstream of the conical body exhibit a pair of counter-rotating vortices due to the free-stream flow entraining into the separating bubble and interacting with the reversal velocities in the low-momentum region behind the body. These vortices are not clearly observed at two to three diameters downstream of the cone where the wake recovery commences.

The instantaneous flow field revealed laminar shear layers forming from the sides of the cone, which separate from the cone's surface shortly downstream. This is especially noticeable along the upper half of the cone. In the near-wake region, the laminar-to-turbulent transition of the shear layers induced the generation of roll-up shear layer vortices. These interacted with the free-stream flow and the enclosed bubble and lose their coherence before the onset of von Karman vortex shedding in the far-wake. Such transition of the dominating flow structures was significantly affected under surface-piercing conditions when the cone's apex was not submerged as the flow near the top of the cone was highly deflected to the sides due to the absence of flow overtopping.

The wake was affected by the transition from emergent (surface-piercing) to shallow submerged flow conditions. As the submergence level increased, changes in the velocity field, instantaneous flow structures, and vortex shedding patterns were more subtle. In line with these results, the Strouhal number and drag coefficient were markedly higher for the emergent condition compared to the submerged conditions, which is also common in cylinder flows. Spectra from wake velocities and cone forces coincide with frequency values corresponding to the highest energy peaks, which indicate that the shear

layer vortices and von Karman vortices are shed at the same frequency.

Overall, despite the geometrical differences between the studied conical island with ellipsoidal shapes and cylinders, such as the inclined walls and pointed free-end, most of the flow phenomena developed around these bluff bodies are consistent in all cases. To date, there is a scarcity of studies that have examined the impact of submergence on the flow structures in the wake of three-dimensional bodies, and this study demonstrates that the key features reported for the flow around a conical island are common to more natural obstacles found in oceanic and geophysical flows.

ACKNOWLEDGMENTS

The authors acknowledge the support of the Supercomputing Wales project, which is part-funded by the European Regional Development Fund (ERDF) via Welsh Government. Furthermore, Dr. Evans wishes to thank Intertek Energy and Water Consultancy Services for their support of this innovative research, and further information can be found at <http://www.intertek.com/energy-water/tidal-energy/>.

- ¹J. Fröhlich and W. Rodi, “LES of the flow around a circular cylinder of finite height,” *J. Heat Fluid Flow* **25**, 537–548 (2004).
- ²D. Chen and G. H. Jirka, “Experimental study of plane turbulent wakes in a shallow water layer,” *Fluid Dyn. Res.* **16**, 11–41 (1995).
- ³M. M. Zdravkovich, “The effect of interference between circular cylinders in cross flow,” *J. Fluids Struct.* **1**, 239–261 (1987).
- ⁴A. Singha, A. M. Shinneeb, and R. Balachandar, “PIV-POD investigation of wake of a sharp-edged flat bluff body immersed in a shallow channel flow,” *J. Fluids Eng.* **131**, 021202 (2009).
- ⁵T. Kawamura, M. Hiwada, T. Hibino, I. Mabuchi, and M. Kumuda, “Flow around a finite circular cylinder on a flat plate,” *Bull. JSME* **27**, 2142–2151 (1984).
- ⁶G. Palau-Salvador, T. Stoesser, and W. Rodi, “LES of the flow around two cylinders in tandem,” *J. Fluids Struct.* **24**, 1304–1312 (2008).
- ⁷N. D. Öztürk, A. Akkoca, and B. Sahin, “Flow details of a circular cylinder mounted on a flat plate,” *J. Hydraul. Res.* **46**, 344–355 (2008).
- ⁸D. Sumner, J. L. Heseltine, and O. J. P. Dansereau, “Wake structure of a finite circular cylinder of small aspect ratio,” *Exp. Fluids* **37**, 720–730 (2004).
- ⁹R. J. Pattenden, S. R. Turnock, and X. Wang, “Measurements of the flow over a low-aspect-ratio cylinder mounted on a ground plane,” *Exp. Fluids* **39**, 10–21 (2005).
- ¹⁰F. Kiani and K. Javadi, “Investigation of turbulent flow past a flagged short finite circular cylinder,” *J. Turbul.* **17**, 400–419 (2016).
- ¹¹G. Palau-Salvador, T. Stoesser, J. Fröhlich, M. Kappler, and W. Rodi, “Large eddy simulations and experiments of flow around finite-height cylinders,” *Flow, Turbul. Combust.* **84**, 239–275 (2010).
- ¹²M. Benitz, D. Carlson, B. Seyed-Aghazadeh, Y. Modarres-Sadeghi, M. Lackner, and D. Schmidt, “CFD simulations and experimental measurements of flow past free-surface piercing, finite length cylinders with varying aspect ratios,” *Comput. Fluids* **136**, 247–259 (2016).
- ¹³H. Wang and Y. Zhou, “The finite-length square cylinder near wake,” *J. Fluid Mech.* **638**, 453–490 (2009).
- ¹⁴P. Sattari, D. Rival, R. Martinuzzi, and C. Tropea, “Growth and separation of a start-up vortex from a two-dimensional shear layer,” *Phys. Fluids* **24**, 107102 (2012).
- ¹⁵R. Martinuzzi and C. Tropea, “The flow around surface-mounted, prismatic obstacles placed in a fully-developed channel flow,” *J. Fluids Eng.* **115**, 85–92 (1993).
- ¹⁶H. Shamloo, N. Rajaratnam, and C. Katopodis, “Hydraulic on simple habitat structures,” *J. Hydraul. Res.* **39**, 351–366 (2001).
- ¹⁷S. Hajimirzaei, C. Wojcik, and J. Buchholz, “The role of shape and relative submergence on the structure of wakes of low-aspect-ratio wall-mounted bodies,” *Exp. Fluids* **53**, 1943–1962 (2012).
- ¹⁸H. Sakemoto and M. Arie, “Vortex shedding from a rectangular prism and a circular cylinder placed vertically in a turbulent boundary layer,” *J. Fluid Mech.* **126**, 147–165 (1983).
- ¹⁹S. Krajnovic, “Flow around a tall finite cylinder explored by large eddy simulation,” *J. Fluid Mech.* **676**, 294–317 (2011).
- ²⁰T. Uffinger, I. Ali, and S. Becker, “Experimental and numerical investigations of the flow around three different wall-mounted cylinder geometries of finite length,” *J. Wind Eng. Ind. Aerodyn.* **119**, 13–27 (2013).
- ²¹M. A. F. Sadeque, N. Rajaratnam, and M. R. Loewen, “Shallow turbulent wakes behind bed-mounted cylinders in open channels,” *J. Hydraul. Res.* **47**, 727–743 (2009).
- ²²P. M. Lloyd and P. K. Stansby, “Shallow-water flow around model conical islands of small side slope. II: Submerged,” *J. Hydraul. Eng.* **123**, 1068–1077 (1997).
- ²³R. Lacey and C. D. Rennie, “Laboratory investigation of turbulent flow structure around a bed-mounted cube at multiple flow stages,” *J. Hydraul. Eng.* **138**, 71–84 (2012).
- ²⁴P. M. Lloyd and P. K. Stansby, “Shallow-water flow around model conical islands of small side slope. I: Surface piercing,” *J. Hydraul. Eng.* **123**, 1057–1067 (1997).
- ²⁵I. Afgan, C. Moulinec, R. Prosser, and D. Laurence, “Large eddy simulation of turbulent flow for wall mounted cantilever cylinders of aspect ratio 6 and 10,” *Int. J. Heat Fluid Flow* **28**, 561–574 (2007).
- ²⁶T. Stoesser, S. Kim, and P. Diplas, “Turbulent flow through idealized emergent vegetation,” *J. Hydraul. Res.* **136**, 1003–1017 (2010).
- ²⁷P. Evans, A. Mason-Jones, C. A. M. E. Wilson, C. F. Wooldridge, T. O’Doherty, and D. M. O’Doherty, “Constraints on extractable power from energetic tidal straits,” *Renewable Energy* **81**, 707–722 (2015).
- ²⁸J. F. Douglas, J. Gasiorek, and J. Swaffield, *Fluid Mechanics*, 3rd ed. (Longman Pub Group, 1995).
- ²⁹D. Goring and V. Nikora, “Despiking acoustic Doppler velocimeter data,” *J. Hydraul. Eng.* **128**, 117–126 (2002).
- ³⁰S. Bomminayuni and T. Stoesser, “Turbulence statistics in an open-channel flow over a rough bed,” *J. Hydraul. Eng.* **137**, 1347–1358 (2011).
- ³¹Y. Liu, T. Stoesser, H. Fang, A. Papanicolaou, and A. Tsakiris, “Turbulent flow over an array of boulders placed on a rough permeable bed,” *Comput. Fluids* **158**, 120–132 (2017).
- ³²J. Smagorinsky, “General circulation experiments with the primitive equations,” *Mon. Weather Rev.* **91**, 99–164 (1963).
- ³³M. Uhlmann, “An immersed boundary method with direct forcing for the simulation of particulate flows,” *J. Comput. Phys.* **209**, 448–476 (2005).
- ³⁴A. Cristallo and R. Verzicco, “Combined immersed boundary/large-eddy-simulations of incompressible three dimensional complex flows,” *Flow, Turbul. Combust.* **77**, 3–26 (2006).
- ³⁵S. Kara, T. Stoesser, T. W. Sturm, and S. Mulahasan, “Flow dynamics through a submerged bridge opening with overtopping,” *J. Hydraul. Res.* **53**, 186–195 (2015).
- ³⁶P. Ouro, M. Harrold, T. Stoesser, and P. Bromley, “Hydrodynamic loadings on a horizontal axis tidal turbine prototype,” *J. Fluids Struct.* **71**, 78–98 (2017).
- ³⁷P. Ouro and T. Stoesser, “An immersed boundary-based large-eddy simulation approach to predict the performance of vertical axis tidal turbines,” *Comput. Fluids* **152**, 74–87 (2017).
- ³⁸B. Fraga and T. Stoesser, “Influence of bubble size, diffuser width and flow rate on the integral behaviour of bubble plumes,” *J. Geophys. Res.: Oceans* **121**, 3887–3904, <https://doi.org/10.1002/2015jc011381> (2016).
- ³⁹B. Fraga, T. Stoesser, C. C. Lai, and S. A. Socolofsky, “A LES-based Eulerian-Lagrangian approach to predict the dynamics of bubble plumes,” *Ocean Model.* **97**, 27–36 (2016).
- ⁴⁰M. Cevheri, R. McSherry, and T. Stoesser, “A local mesh refinement approach for large-eddy simulations of turbulent flows,” *Int. J. Numer. Methods Fluids* **82**, 261–285 (2016).
- ⁴¹J. Fröhlich, C. Mellen, W. Rodi, L. Temmerman, and M. Leschziner, “Highly resolved large-eddy simulation of separated flow in a channel with streamwise periodic constrictions,” *J. Fluid Mech.* **526**, 19–66 (2005).
- ⁴²J. Hunt, C. Abell, S. Peterka, and H. Woo, “Some aspects of three-dimensional separation. Part 1. Stream surface bifurcations,” *J. Fluid Mech.* **86**, 179–200 (1978).
- ⁴³D. Sumner, “Flow above the free end of a surface-mounted finite-height circular cylinder: A review,” *J. Fluids Struct.* **43**, 41–63 (2013).
- ⁴⁴T. Stoesser, “Large-eddy simulation in hydraulics: Quo vadis?,” *J. Hydraul. Res.* **52**, 441–452 (2014).